Rate-Equation Modeling of Xe and Kr TALIF for Electric Propulsion Applications

IEPC-2022-298

Presented at the 37th International Electric Propulsion Conference
Massachusetts Institute of Technology, Cambridge, MA USA
June 19-23, 2022

Tad Wegner[1], Ciprian Dumitrache[2], Azer P. Yalin[3]
Colorado State University, Fort Collins, CO, 80523, USA

Two-photon absorption laser induced fluorescence (TALIF) is a laser diagnostic technique which can, in principle, provide ground-state density measurements of atoms (e.g., Kr, Xe, N, O) in plasma, flames and reacting flows. Our focus is on application of TALIF to low density plasmas, including those of interest in electric propulsion (EP) research, e.g., the plume of a Hall effect thrusters (HETs), for quantitative neutral density measurements. We develop a 5-level rate-equation model using published rates to examine how the laser field drives the population levels and generates the fluorescence signal. We examine dependences of TALIF signal on laser intensity, pulse energy, and focusing conditions, including the role of photoionization in depleting the signal. We compare model predictions to experimental data for the temporally decaying fluorescence profile and overall TALIF signal levels. Issues related to TALIF detection in plasmas, as well as a comparison of the strength of Xe and Kr TALIF, as is relevant to EP studies, are also considered. The model is specifically formulated for transitions in Xe and Kr but is readily extensible to other species and transitions

I. Introduction

Laser Induced Fluorescence (LIF) is a widely used laser diagnostic that has been applied to many fields including plasma diagnostics, combustion, reactive flow field measurements, and atmospheric science [1, 2]. In the LIF technique, a collection of atoms (or molecules) absorbs incident laser light causing them to be promoted to a higher energy level that then undergoes spontaneous emission down to a lower state. The emitted light, referred to as fluorescence, is collected with a detector and can be analyzed to infer properties of the flow field, for example, velocities from Doppler shifts, temperatures from lineshapes or Boltzmann ratios, and (absolute) densities from signal levels. In this contribution we are focused on diagnostics of low density gases and plasmas, particularly in connection with electric propulsion (EP) research and applications, for example, the low density gas and plasma in the environment of a Hall effect thruster (HET) or gridded ion thrusters [3]. LIF has been applied to these EP systems, most commonly for velocity measurements of xenon atoms and ions (e.g., [4, 5]) using approaches similar to those developed for fundamental studies of sheaths in low temperature plasmas [6]. While these LIF schemes are well suited for velocimetry, they are generally not appropriate for overall density measurements (of neutral atoms or ions) as are also needed by the community. The issue is that the (starting) lower-states used in these LIF schemes (e.g., of Xe or Xe^+) typically correspond to excited states (often metastable). The low-population fractions of these excited states (typically ~0.1-1% of the overall species) reduce signal levels but, more problematically, severely hinders the ability to infer the overall species population given the exact population fraction tends to vary sensitively with local plasma conditions [7, 8]. For many atoms of interest, direct probing of the ground-state (containing a high fraction of the overall population) is not practical because the needed optical transitions are too far in the vacuum ultraviolet (VUV) or x-ray region for practical laser sources. Laser absorption experiments using VUV synchrotron radiation in

---

[1] Graduate Research Assistant, Department Mechanical Engineering, tad.wegner@colostate.edu.

[2] Assistant Professor, Department Mechanical Engineering, ciprian.dumitrache@colostate.edu.

[3] Professor, Department Mechanical Engineering, azer.yalin@colostate.edu.

plasma have been performed for atomic N and O in a radio-frequency plasma; however, the technique lacks spatial and temporal resolution and requires specialized facilities [9].

Direct probing of atomic ground states can often be achieved with Two-Photon Absorption Laser Induced Fluorescence (TALIF) spectroscopy, a variant of LIF where the where the first absorption (excitation) step is based on two-photon absorption (as opposed to typical single-photon). Two-photon absorption is a non-linear optical process first theorized by Goeppert-Mayer in 1931 in which two-photons are simultaneously absorbed by an atom (electron), exciting it to an upper state with an energy gap equal to the sum of the energies of the two photons (and the rate scaling with the square of laser intensity) [10]. Given the energy level spacing issue mentioned above, there are many cases where TALIF allows direct probing of ground-states but with practical laser sources operating in the ~200-250 nm ultraviolet region (e.g., with frequency-doubled or -tripled dye lasers or optical parametric oscillators (OPOs)). Next, we provide a brief overview of past work using TALIF to study plasmas, flames and related systems.

Within the EP field there has been substantial research towards using TALIF to measure neutral propellant atoms, particularly xenon (Xe), to address issues such as propellant utilization fraction and role of charge-exchange reactions. In 1996, Crofton probed Xe with two-photon absorption at 225.4 nm (to excited state $[^2P^0_{3/2}]$ 7p $[3/2]_2$) in the T5 ion thruster plume to measure the axial xenon density profile, reporting a non-linear density decay away from the thruster [11]. In 2007, Eichhorn et al. made comparative measurements of TALIF signals of Xenon in a cold gas cell using wavelengths of 224.2, 225.4 nm, and 226.4 nm finding that the 3 excitation schemes yielded similar strength signals [12]. Subsequently in 2013, Crofton et al. used the 222.5 nm Xe TALIF line to perform a detailed measurement of the radial and axial neutral density distribution in the plume of the SP-140 4.5 kW Hall thruster [13]. In 2019, Kinefuchi et al. performed a similar study in a cold xenon gas, evaluating the 249.5 nm and 252.5 nm lines and measuring spontaneous decay rates for both lines [14]. Building upon these efforts, recent work from our research group has shown HET measurements of a 1.5 kW thruster using the 222.5 nm excitation scheme [15, 16]. To the best of our knowledge, despite the growing interest in using Krypton as a propellant in EP research (owing in part to the very high cost of xenon currently), TALIF detection of Kr has not yet been reported in EP-related studies. On the other hand, Kr-TALIF has been developed as a flow-tracer in flames [17] and for flow-tagging velocimetry for supersonic and hypersonic flow [18-22]. These applications rely on the inert nature of Kr but are generally at higher pressures (>~1 mbar) than those of EP interest, meaning that quenching becomes more prevalent and effects such as generation of dimer ions likely play a role [23]. There have also been limited Kr TALIF studies in low temperature plasma sources, e.g. by Galante et al. to probe neutral density profiles in helicon plasmas [24].

The inert nature of Xe and Kr also makes it possible to have fixed amounts of these gases within reference cells as a means to calibrate TALIF density measurements of reactive species, such as atomic oxygen (O) or nitrogen (N), in plasma discharges. Atomic O and N represent primary kinetic pathways for the generation of most reactive species of interest in air plasmas and are thus of interest in many applications including plasma processing, biomedicine, bio-decontamination, plasma-assisted combustion, and aerodynamic flow control [25-27]. Major progress towards quantitative measurements was made by Niemi et al. [28] who determined several relevant two-photon absorption cross-sections. The overall calibration method is based on comparing the TALIF signal for N or O atoms with spectrally proximate TALIF schemes in either Kr or Xe [29]. A ratio approach between the TALIF signals due to the two species allowing cancellation of many experimental constants (e.g. solid angle or collection efficiency). However, care must be taken to properly accommodate variation in laser energy between measurements. Related recent work has investigated potential benefits of TALIF with fs-sources versus widely used ns-sources. Schmidt et al. have shown that fs-TALIF reduces the presence of photolytic interference at high laser fluences and enables 2D imaging of atomic species [30, 31]. Dumitrache et al. demonstrated that fs-TALIF can be performed in a quench-free regime by depopulating the excited state before the end of the pulse using the strong photoionization effect induced at high laser intensities [32].

Earlier TALIF modeling efforts have focused on obtaining cross-section data from calibration experiments. One of the first such studies was by Bamford et al. [33] where the authors propose a 4-level generic rate model for TALIF involving the ground state, the two-photon excited state, the fluorescence decay intermediate state and, importantly, photoionization by absorption of a third photon from the excited state. This study identifies three fluorescence regimes: *i*) a low intensity regime ($I_{laser} < 25$ MW) where the population of ground state remains virtually unchanged and the fluorescence signal scales as $\sim I_{laser}^2$; *ii*) an intermediate intensity regime ($I_{laser} \sim 25 - 1500$ MW) in which the contribution from photoionization can be observed; and *iii*) and finally a high intensity regime ($I_{laser} > 1500$ MW) where the authors hypothesize that the rate model approach must be replaced by a density matrix analysis due to the presence of AC Stark shifting of the lines (which is expected to limit the ionization fraction). This hypothesis was later confirmed by the modeling effort of Stancu [34]. Comparing the results from the density matrix model for O-atom TALIF with the standard rate model, the author noted significant disagreement at intensities above 10 GW/cm^2.

The remainder of the paper is laid out a follows. Section 2 discusses the equations and rates used in the 5-level rate equation model. Section 3 gives a short summary of the experimental setup used to obtain low-density TALIF data. Section 4 presents results and discussion, including examining TALIF intensity regimes, the roles of photoionization, fluorescent decays and signal dependences on pulse energy and focusing. Finally, conclusions are provided in Section 5.

II. Rate-Equation Model

A generic energy level diagram describing the main processes involved in TALIF experiments is presented in Fig. 1 below. The model considers 5 levels: the ground state (which is also the lower state of the 2-photon absorption), the TALIF fluorescence upper level (which is also the upper state of the 2-photon absorption), the TALIF fluorescence lower levels (i.e., the levels to which the fluorescing photons decay), and a higher-lying ionized state (which is populated by photoionization out of the fluorescence upper state at high laser intensity). These levels are denoted E_0, E_2, $E_{1,1}$, $E_{1,2}$ and E_i respectively, with populations (per unit volume) n_0, n_2, $n_{1,1}$, $n_{1,2}$ and n_i respectively. This same scheme can be applied to multiple transition schemes in Xe and Kr (and N and O). This model formulation assumes that the upper fluorescence state E_2 has two radiative channels to lower states (one of which, $E_{1,1}$, is used for TALIF detection); in cases where there are more (or less) such channels then other $E_{1,i}$ states can be added (or removed) accordingly.

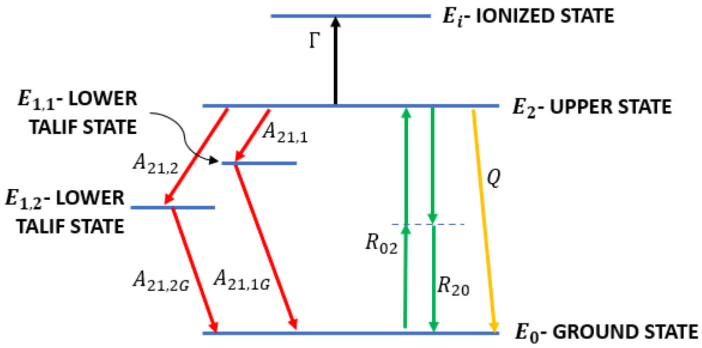

Figure 1: Generic energy level diagram showing the transitions and the rates for the 5-level TALIF model.

The 5-level TALIF rate equation model presented here can be used for different atoms and different transitions (different E_2 and $E_{1,i}$) for a given atom. We have configured the model for two representative cases of interest in plasma (EP) research, one for xenon atoms and one for krypton atoms. The rates used are shown in Table 1 (with references) and the specific energy level diagrams are shown in Figure 2. In the case of Xenon we have two-photon excitation (222.5 nm) from the ground state 5s^2 5p^6 $^1S_0$ to the 6p'[1/2]$_0$ upper state (~89,860 cm^{-1}), from which we detect TALIF fluorescence ($A_{21,1}$) at 788.7 nm to the ($^2P^0{}_{1/2}$) 6s'[1/2]$^0{}_1$ lower level (~77,185 cm^{-1}). Here, we use the Racah notation for depicting the energy levels of Xe. In this case, there is 1 other fluorescence channel ($A_{21,2}$) out of the same upper fluorescence level, which is at wavelength 458 nm to the ($^2P^0{}_{3/2}$) 6s ^{2}[3/2]$^0{}_1$ lower level (~68,045 cm^{-1}). Both of these lower levels ($E_{1,1}$ and $E_{1,1}$) have strong resonance transitions to the ground state (via $A_{21,1G}$ and $A_{21,2G}$). Note there are a series of other similar Xe TALIF schemes with 2-photon excitation from the ground state but to either different levels of the 6p' manifold (and then fluorescing to 6s' states) or to levels of the lower lying 6p manifold (and then fluorescing to the 6s manifold) [12, 35, 36]. As will be further discussed in Section 4.3, the 222.5 nm scheme adopted here has been used successfully in experimental HET measurements.

The spectroscopy of Kr is relatively similar to that of Xe, where for Kr we use two-photon excitation (214.7 nm) from the ground state 4s^2 4p^6 $^1S_0$ to the 5p ^{2}[3/2]$_2$ upper state (~93,123 cm^{-1}), from which we detect the TALIF fluorescence ($A_{21,1}$) at 760.2 nm to the 5s ^{2}[3/2]$^0{}_2$ lower level (~79,972 cm^{-1}). In this case, there is 1 other fluorescence channels ($A_{21,2}$) from the upper fluorescence level at wavelength 819 nm to the 5s ^{2}[3/2]$^0{}_1$ lower level (~80,917 cm^{-1}). The lower level of the TALIF transition is a metastable state with very weak transition rate ($A_{21,1G}$) back to the ground-state, while the lower level of the 819 nm channel has a strong rate ($A_{21,2G}$) back to the ground state. This is the main qualitative difference between the selected Xe and Kr TALIF schemes (i.e., both lower fluorescent levels decay strongly to the ground state for Xe, whereas in the case of Kr, the lower level of the TALIF emission is metastable). There are a series of other Kr TALIF schemes with 2-photon excitation from the ground state but to either different levels of the 5p manifold (and then fluorescing to the same two 5s states) or to levels of the higher lying 5p' manifold (and then fluorescing to the two states of the 5s' manifold) [37, 38].

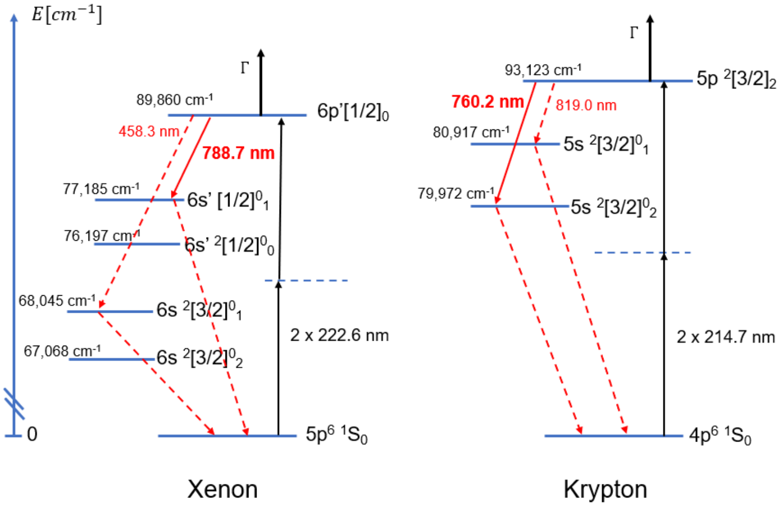

Figure 2: TALIF energy-level diagrams for Xe (left) and Kr (right) showing specific TALIF levels and wavelengths. Red lines indicate radiative transitions with the solid red line showing the TALIF detection.

In a typical laser fluorescence experiment, one is interested in determining the density of the ground state from the measured fluorescence signal. Numerically, the populations can be obtained by solving the following rate equation model:

$$
\begin{aligned}
\frac{dn_0}{dt} &= -R_{02}(t)n_0 + (R_{20}(t) + Q)n_2 + A_{21,1G}n_{1,1} + A_{21,2G}n_{1,2} \\
\frac{dn_2}{dt} &= R_{02}(t)n_0 - \big(R_{20}(t)n_2 + A_{21,1} + A_{21,2} + Q + \Gamma(t)\big)n_2 \\
\frac{dn_{1,1}}{dt} &= A_{21,1}n_2 - A_{21,1G}n_{1,1} \\
\frac{dn_{1,2}}{dt} &= A_{21,2}n_2 - A_{21,2G}n_{1,2} \qquad (1) \\
\frac{dn_i}{dt} &= \Gamma(t)n_2 \\
n_{tot} &= n_0 + n_{1,1} + n_{1,2} + n_2 + n_i
\end{aligned}
$$

where R_{02} represents the two-photon absorption rate from the ground state to the fluorescence upper state, R_{20} is the two-photon stimulated emission process between the same states, $A_{21,1}$ is the TALIF emission rate (i.e., Einstein coefficient of the transition for fluorescence detection) from the fluorescence upper state, $A_{21,2}$ is the emission rate of the second (other) fluorescence channel from the fluorescence upper state, and $A_{21,1G}$ and $A_{21,1G}$ are the emission rates from the intermediate levels $n_{1,1}$ (lower level of TALIF fluorescence) and $n_{1,2}$ (lower level of the other fluorescent channel) to the ground state respectively. $\Gamma(t)$is the time-dependent photoionization rate from n_2 to n_i and Q is the quenching rate from n_2 to n_0. All the rates explicitly balance such that n_{tot}, found as the sum of all contributing populations, is conserved.

Detailed rates are provided in Table 1 below. The two-photon absorption rate is:

$$R_{02}(t) = \sigma^{(2)}{}_{\nu}\left(\frac{I_{Laser}(t)}{h\nu}\right)^{2} \tag{2}$$

$$R_{02}(t) = \sigma^{(2)} g_L(\nu) G^{(2)} (I_{Laser}(t)/h\nu)^2 \tag{3}$$

where $\sigma^{(2)}{}_{\nu}$ (units: $\mathrm{cm}^4\mathrm{s}$) is the (frequency integrated) two-photon absorption cross-section and $I_{Laser}(t)$ is the laser intensity profile. In Eqn. (3), the cross-section is recast in terms of the laser pulse characteristics. Here, $\sigma^{(2)}$(units: cm^4) is the two-photon absorption cross-section [38, 39], $g_L(\nu)$ is the absorption lineshape, which depends on various broadening mechanisms (e.g., thermal, pressure, instrumental, etc.), denoted together as φ_{Abs}, and the laser lineshape, denoted as φ_{Laser}, as: $g_L(\nu) = \varphi_{Abs} \otimes \varphi_{Laser} \otimes \varphi_{Laser}$. The laser profile convolution is performed twice since the process of absorption involves the simultaneous absorption of two laser photons. It is likewise important to observe that, for applications involving the use of a spectrograph for resolving the emission, one may also need to include the instrumental broadening of the spectrograph within φ_{abs}. Alternatively, the absorption lineshape can also be determined from experimental TALIF data. In particular, the value of the (normalized) lineshape evaluated at the peak of the TALIF transition can be found from the full TALIF lineshape as: $g_L(\nu_{pk}) = F_{pk}/\int_{-\infty}^{+\infty} F(\nu) d\nu$, where $F(\nu)$ is the experimental TALIF absorption lineshape found by scanning the laser across the peak. Based on experimental data with the dye laser used for Xenon in the present work (Section 3) we find a value of $g_L(\nu_{pk}) = 5 \times 10^{-11}\mathrm{s}$.

The photon statistics factor is explained in detail in other works [34, 35]. Briefly, the absorption efficiency depends on the temporal profile of the laser pulse. When the laser intensity is measured experimentally (e.g., with a photodiode) it is important to realize that one does not really measure the (true) quickly oscillating intensity, $I(t)$, but rather the average intensity over an integration window dictated by the bandwidth and response time of the electronics (order ns). The consequence of this, given also the TALIF dependence on the square of the laser intensity, is a photon statistics factor that corrects between the measured and real squared intensity profile. For a true single-mode laser the photon statistics factor is $G^{(2)} = 1$. For a typical Nd:YAG laser the factor has been estimated to be $G^{(2)} \sim 2$, which is the value we adopt here [40]. (Note that care must be taken to use similar lasers between different setups for ratio-based calibrations, given the uncertainty in this parameter.)

The quenching rate (due to 2-body collisions) is defined as:

$$Q = \sum_{l} k_l n_l \tag{4}$$

where k_l (units: $\mathrm{cm}^3\mathrm{s}^{-1}$) is the collider quenching coefficient (with index "l" for different collision partner species of density n_l). Here, we consider only single-component gases so the sum reduces to a single term. Quenching coefficients for xenon and krypton are provided in Table 1.

The photoionization rate is given by:

$$\Gamma(\mathrm{t}) = \sigma_{ph}(I_{Laser}(t)/h\nu) \tag{5}$$

where σ_{ph}(units: cm^2) is the photoionization cross-section for atoms in level E_2 (to E_i). The photo-ionization cross-sections are provided in Table 1. For Xenon, we could not find rates for the exact 6p'[1/2]$_0$ upper state and so we estimated it by taking the average of the similar 6p[1/2]$_0$ state reported by Kroll and Bischel at 193 nm and 248 nm excitation wavelengths [35]. For krypton, we use published rates for 5p states [41].

Table 1: Parameters and rates used in 5-level TALIF rate-equation model.

	Xe	Kr
$\lambda_{\text{2-photon}}$ [nm]	222.5	214.7
λ_{Fluor} [nm]	788.7	760.2

$\sigma^{(2)}$ [cm^{-4}]	4.94×10^{-34} [39]	4.18 x 10^{-35} [38]
$g(\nu_{pk})$ [sec]	5×10^{-11}	5×10^{-11}
$G^{(2)}$	2	2
K [cm^3 sec^{-1}]	1×10^{-10} [42]	1.7 x 10^{-10} [23]
$A_{21,1}$ [1/sec]	3.5×10^7 [43]	2.73 x 10^7 [43]
$A_{21,2}$ [1/sec]	1.3×10^6 [43]	8.94 x 10^6 [43]
$A_{21,1G}$ [1/sec]	2.53×10^8 [43]	3.54 x 10^{-2} [43]
$A_{21,2G}$ [1/sec]	2.73×10^8 [43]	2.98 x 10^8 [43]
σ_{ph} [cm^2]	3×10^{-18} [35]	4.5 x 10^{-18} [41]

We also model the amplitude of the total (non spectrally-resolved) fluorescence signal, *F(t)*, expressed as the # of photons emitted per unit volume and per unit time:

$$F(t) = N_2\, A_{21} \qquad (6)$$

as well as the total # of fluorescent photons detected in a fluorescent event, F_{total}, which is found by time-integrating the fluorescence signal and also considering the collection volume and collection system:

$$F_{Total} = \frac{\Delta\Omega}{4\pi} V\eta \int_0^t F(t)dt \qquad (7)$$

where $\Delta\Omega$ is the collection solid angle (sr), V is the collection volume, η is the combined efficiency of the detector and collection optics, and the time-integration is performed over the extent of the fluorescence signal. Based on typical experimental values, we adopt $\Delta\Omega$=0.012 and η=0.1. (Detection efficiencies between Xe and Kr may also vary due to the wavelength of the detected lines, but we neglect this here.) The volume of the collection region is computed as an ellipsoid, where the two minor axes have radii equal to the beam waist and the major axis (aligned with the direction of the TALIF laser) is taken as the confocal beam parameter (but with maximum of 3 mm in cases where the confocal parameter exceeds that).

III. Experimental

We have recently performed TALIF of xenon using a dye laser, both in reference cells and in the plume of a HET operating in a vacuum chamber, and leverage some of those results for validation of the TALIF model. The experimental setup for light delivery is shown in Fig. 3. The dye laser system comprised the third harmonic (355 nm) of an Nd:YAG laser (Continuum Surelite III) as the pump source for the actual dye laser module. The laser operated with Coumarin 440 dye to generate a visible output beam at ~445 nm which was passed to the frequency-doubler (Vista FX) to achieve the desired output wavelength in the vicinity of 222.5 nm. The beam was then directed from the optical table exterior to the chamber via steering mirrors (Lattice Optics RX-225-45-UF-1025) through an Anti-Reflecton coated window (ThorlabsVPCH42-UV) into the chamber. Inside the chamber, a 500 mm focusing lens (Thorlabs LA4184) brought the beam to a weak focus at the measurement location. On the far end of the chamber a black carbon sheet acted as a beam dump. The collection lens (Newport KBX160AR.16) was placed 300 mm below the beam focus and the collection mirror (Thorlabs BB2-E03) reflected the collected light into an optical fiber (Thorlabs M29L02). The collection lens was positioned for 3:1 imaging (with the larger dimension of 1.8 mm on the side of the TALIF beam and smaller dimension of 0.6 mm matched to the fiber diameter). This light was passed through a fiber feedthrough (Thorlabs VC2L6S) which was connected to a second identical fiber exterior to the chamber. The output of the second fiber was sent directly into the PMT (Hamamatsu R3896) with a bandpass filter (Thorlabs FB790-10).

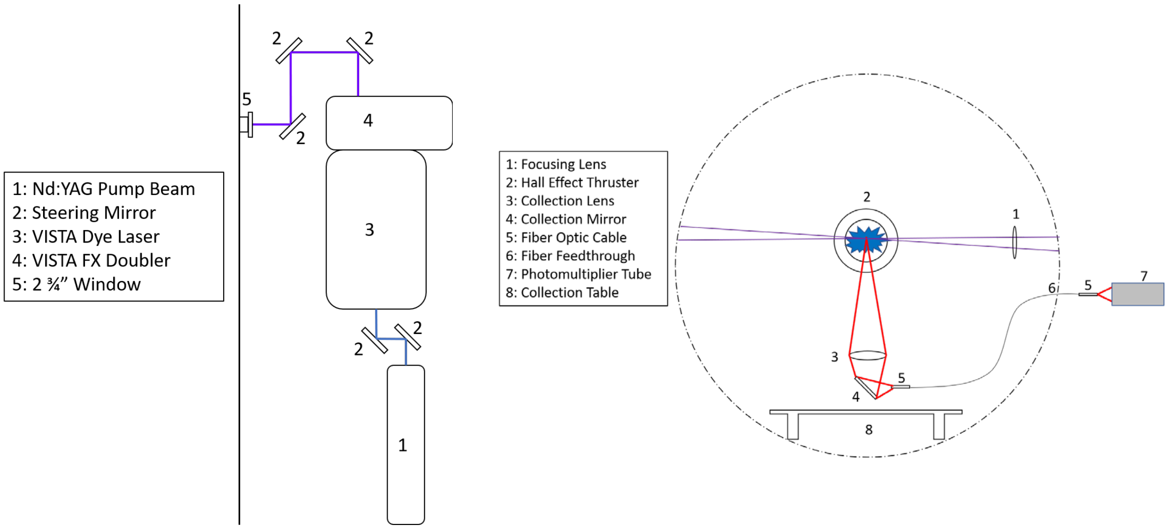

Figure 3: Schematic of experimental setup. Left: Air-side setup showing beam delivery. Right: Vacuum-side setup showing TALIF focusing, TALIF light collection, and Hall effect thruster.

The focused beam waist at the measurement location was determined to be approximately 1.3 mm based on a knife-edge experiment. Therefore, the entire width (transverse dimension) of the beam focus could be imaged, while light is collected along a beam extent of ~1.8 mm in the axial direction. Competing luminosity (from the same and nearby optical transitions as detected in LIF) cause a plasma background emission signal which limits the PMT signal levels – see discussion in Section IV-C.

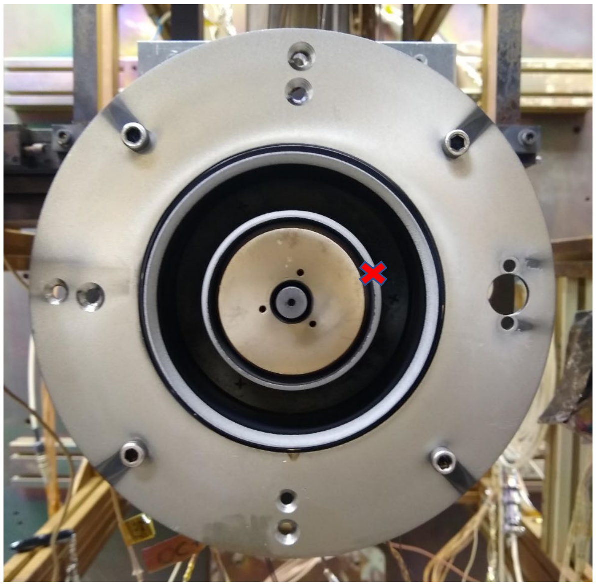

Figure 4: 1.5 kW Hall thruster with red X marking the approximate TALIF measurement location.

The thruster was a 1.5 kW SPT style thruster with a ceramic borosil (BN-SiO2) channel. The channel dimensions were 104 mm O.D. with a width of 17 mm and a length of 32 mm (V = 150 cm^3). Four outer coils coupled with a center coil generate the magnetic field in the channel. A center-mounted heaterless hollow cathode ignites and feeds the plasma through electron emission and minimizes plume divergence (~20° half angle). Measurements were recorded at several axial positions downstream of the thruster face.

The vacuum test facility is comprised of a 1.7 m diameter by 4.6 m long cylindrical chamber pumped by a Leybold DryVac 650 roughing pump and two Varian HS20 diffusion pumps. High purity (99.999% pure) xenon propellant was fed through anode and cathode gas inlets via stainless steel feed lines from a compressed gas bottle. Brooks 5850E mass flow controllers (± 2% accuracy) were used to control the mass flow rate. A Granville Phillips S260 ion gauge (± 25% accuracy) was used to monitor low chamber pressures. The thruster had a range of operating parameters as follows: Thrust: 70 – 100 mN, Specific Impulse: 1500 – 1750 s, Power: 1.3 – 1.8 kW, and Mass flow rate: 3.25- 5.6 mg/s. Past studies have shown neutral density profiles peaking near the thruster channel inner and outer walls. This work has therefore focused on measurement locations roughly coincident with the outer channel wall as shown in Figure 4.

In some cases, TALIF measurements of reference cells have also been performed. The cell measurements (to calibrate the HET measurements) used the identical light delivery and collection as the HET measurements, just with the chamber open and the cell affixed within the chamber (with the laser focus roughly in the center of the cell). Several cells of varying xenon density were used, for example, He-Xe buffer gas at 10 ppm Xe with pressure of 1.52 torr.

IV. Results and Discussion

Here we present general findings from the model along with experimental comparisons including examining TALIF signal dependence on laser intensity, pulse energy and beam diameter, and comparison of Xe and Kr TALIF signals. An outlook and discussion of measurements in the presence of plasma is also presented.

A. Intensity Regimes and Role of Photoionization

Following Bamford et al. [33] we consider different regimes of laser intensity in terms of how the populations are driven by the laser and the resulting TALIF signal. Figure 5 shows modeled level populations and fluorescent signals as found with the 5-level model for Xenon for 3 different laser peak intensities of 5 MW/cm^2, 50 MW/cm^2, and 500 MW/cm^2. The laser is assumed to have a Guassian temporal pulse with FWHM of 12 ns (with intensity peak at time of 20 ns). The initial density (all in the ground state) is taken as $n_0(0)=10^{12}$ cm^{-3}. Other rates and constants are given above. Results for I_{laser}=5 MW/cm^2 are representative of the low intensity regime (I_{laser}<~10 MW/cm^2) where there is only weak excitation of level populations and most of the population remains in the ground state. The fraction of species pumped to n_2 (upper fluorescent level) remains small (n_2/n_{tot} ~ 0.01 for I_{laser}=5 MW/cm^2) and the photoionization rate remains small compared to the two-photon rate so there is minimal ion creation (n_i/n_{tot} ~ 0.001 for I_{laser}=5 MW/cm^2). This regime of weak excitation has some similarity to the "linear-regime" in single-photon LIF experiments [1] though for TALIF signals scale with the square (instead of first power) of laser intensity. In this regime, the fluorescent decays remain as pure exponentials with decay time given by the inverse of the Einstein A-coefficient (i.e., by $A_{21,1}$ for the observed TALIF feature). We also show overlaid experimental data, and exponential fit to the data, obtained from TALIF experiments in our laboratory using this 222.5 nm / 788. nm scheme [15, 16]. The measurements were performed with the setup discussed in Section 3 at low intensity conditions (pulse energy of ~0.3 mJ which with other given parameters yields I_{laser}=~1.9 MW/cm^2). The vertical scale has been adjusted to match the simulation. An exponential fit to the data gives a 1/e time of 26.9 ns which is within good agreement with the expected value of 28.6 ns (=1/ $A_{21,1}$ =1/3.5x10^7 s) given our experimental uncertainty.

The middle panel shows results for I_{laser}=50 MW/cm^2 representative of the medium intensity regime (10 MW/cm^2 <~ I_{laser} <~ 100 MW/cm^2) where there is only weak excitation of level populations and most of the population remains in the ground state. In this regime, rates of two-photon excitation and photoionization are high enough to significantly affect the population distribution. At I_{laser}=50 MW/cm^2, the fluorescent level has (peak) fractional population of ~0.23 and the ion population peaks yet higher at ~0.35. Saturation effects start to occur and the fluorescent decay is no longer a pure exponential (given the competing processes that populate and depopulate E_2). While we do not directly observe the ionized species in our experiments, the laser induced ionization has been observed through microwave scattering experiments from laser excited xenon gas by resonant enhanced multi-photon ionization (REMPI) [44]. Finally, at yet higher intensities (I_{laser}>~100 MW/cm^2) one has a strongly saturated regime as shown with the I_{laser}=500 MW/cm^2 case. In this regime, photoionization strongly dominates (n_i/n_{tot} increases to >0.99 for I_{laser}=500 MW/cm^2). The upper fluorescent level (n_2) population peaks at earlier times and the fluorescent decay signal appears significantly earlier and with a shorter decay. While quenching is negligible at the low-density conditions we have modeled, the high intensity regime is interesting for higher-pressure quench-free diagnostics since the quench rate has negligible effect on strongly saturated signals. As has been discussed in related works [33, 34], the rate-equation approach loses its validity in the strongly saturated conditions where time-dependent Stark shifts of eigen states are important in strong laser E-fields. This leads to an uncertainty in the two-photon cross-section due to the transition energy becoming detuned. In addition, coherent excitation processes and stimulated emission (caused by an inversion of population) as well as Rabi oscillations become important and lead to errors if not properly accounted for. Including these effects, one expects a significant oscillation in the number density of upper levels. In fact, past modelling efforts using a density matrix approach which properly accounts for these processes have been able to confirm the time-resolve fluorescence signal oscillation in the very high intensity regime [34]. The reduction in TALIF signal due to saturation, and related experimental observations, are further examined below.

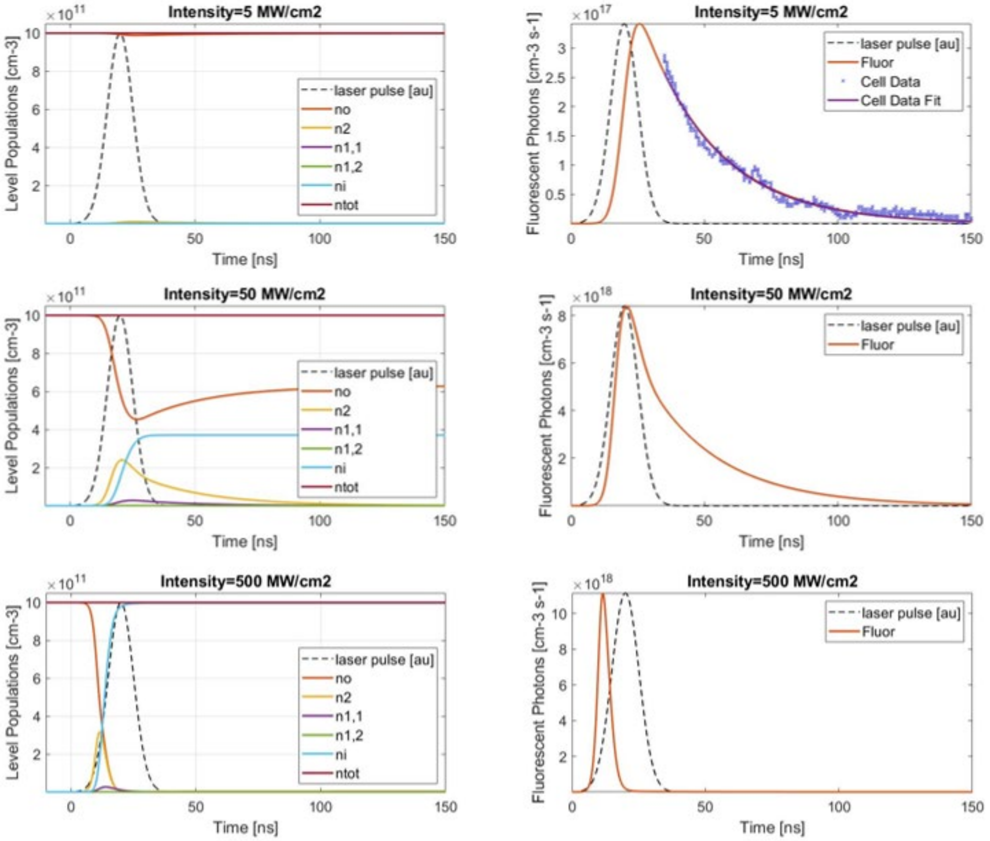

Figure 5: Modeled time-evolution of level populations (left) and fluorescence signals (right) for Xenon TALIF for intensities of 5, 50 and 500 MW/cm^2.

B. Energy Dependence, Focusing, and Signal Saturation

We have also examined the time-integrated total fluorescence signals (expressed as number of detected photons) using equation 7 for Xenon with the parameters given above. The left of Figure 6 shows the fluorescence versus laser intensity along with parabolic and linear fits. In the low intensity regime where the level populations change only weakly the signal increase is well described with an $\sim I^2$ relationship (because the signal scales as $\sim n_2 \sim R_{02}$). Moving to intermediate intensities, the rate of signal increase reduces as saturation effects onset. In this regime, although there is no rigorous basis, data are relatively well fit with a linear dependence over roughly 1 octave (factor of 2) of laser intensity, with example linear segment shown in the plot. As laser intensity further increases, the total fluorescent signal is predicted to decrease due to strong photoionization. This finding is qualitatively different from saturation (bleaching) in single-photon LIF where, for high laser intensity, the signal asymptotes to a constant (maximum) level. The right of Figure 6 compares modeled fluorescence signals to experimentally observed values. The experimental data are taken from 3 campaigns (one measuring the reference cell, and two measuring in HET plume) and have been scaled in amplitude to match the model. In order to achieve the agreement shown in the plot, it was necessary to slightly weaken the saturation onset in the model which was achieved by setting the beam diameter to 0.8 mm (whereas the experimental value was ~0.65 mm). It appears these data correspond to the rising limb of the fluorescent curve as it approaches saturation. There are several reasons that can explain the weaker saturation in experiments versus the model, in particular, and as is also the case with regular 1-photon fluorescence, it is difficult experimentally to achieve full saturation in the temporal and spatial wings of the beam (and the 0-D model does not account for the spatial intensity variations). It is also possible that the multi-mode nature of the beam further weakens the saturation

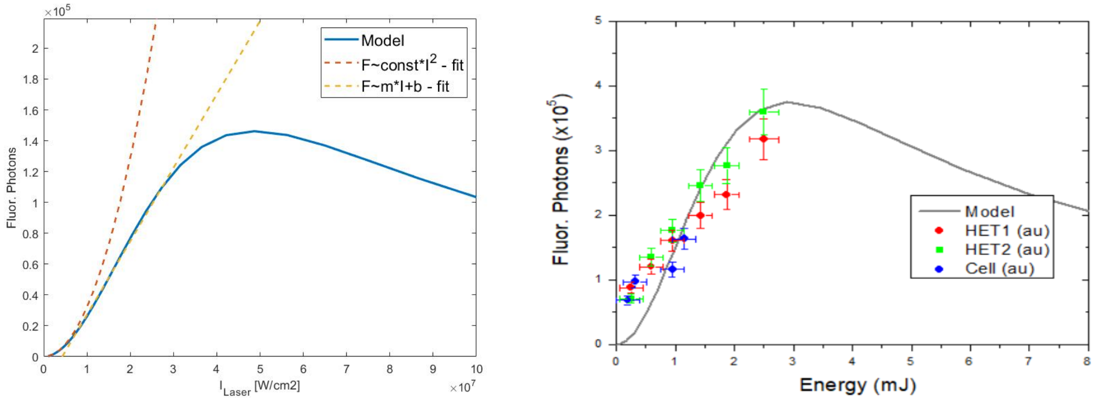

Figure 6: Left: Modeled total (time-integrated) fluorescence versus laser intensity. Right: Modeled total fluorescence versus laser pulse energy with overlaid experimental data.

In considering TALIF experimental scenarios the beam diameter, and focusing, should also be considered. Figure 7 shows surface plots of the base-10 logarithm of the peak (top panels) and total fluorescent signals (bottom panels) as a function of both pulse energy and beam diameter for xenon and krypton. The peak fluorescent signal (#photons cm^{-3} s^{-1}) is found as the peak value over the fluorescent event due to eqn. (6) and is plotted with (base 10) logarithm since signals vary over orders of magnitude. The total detected fluorescent signal (#detected photons) is found from eqn. (7) and also plotted logarithmically. The combination of energy and beam diameter determine the beam intensity which influences the TALIF signal and drives the peak fluorescence signal. The inclined contours in the peak-fluorescence plots (top panel) simply correspond to the beam intensity. As can also be seen from the fluorescent decay profiles in the right of Figure 5, the peak signal monotonically increases with beam intensity (higher energies and smaller beam diameters). The behavior of the total fluorescent signal (bottom panel) is different due to the time-integration of the fluorescence (which tends to get shorter at higher intensity) and because this is also proportional to the scattering volume which varies with the beam diameter (eqn. (7)). Larger beam diameters cause significantly larger scattering volumes since the confocal beam parameter (Rayleigh range) increases. The bottom panel of Figure 5 shows that at constant beam diameter, as the pulse energy increases the TALIF signal goes through a maximum and then reduces; this behavior is the same intensity dependence examined in Figures 5 and 6. Similarly, at fixed energy, e.g. 1 mJ, then as the beam diameter increases the TALIF signal also first increases (due to the rapid growth in volume exceeding the effect of lowering the intensity) but then later decreases (due to intensity becoming too low, despite the large volume).

The results of Figure 7 can guide the selection of experimental TALIF conditions relative to saturation. We also find that for fixed conditions, the (peak or total) TALIF signals for xenon are roughly an order of magnitude higher than those for krypton. This is primarily driven by the higher 2-photon cross-section for the xenon transition (see Table 1) given the other parameters are quite similar. More precisely, one can estimate the Xe:Kr TALIF signal ratio for low laser intensity as $(R_{02} \cdot \phi)_{Xe}/(R_{02} \cdot \phi)_{Kr}$, where ϕ is the fluorescent yield ($=A_{21,1}/(A_{21,1}+A_{21,2}+Q)$) and the quantities are evaluated for Xe and Kr accordingly. For our transition scheme (Table 2), the ratio is 16.2 and dominated by the ratio of the 2-photon cross-sections ($\sigma_{Xe}^{(2)}/\sigma_{Kr}^{(2)}$=12.7), which is consistent with the data of Figure 5. Note that at the low densities of interest, e.g. as in EP experiments, quenching has a negligible affect on signal levels (true up to densities of ~3.5x10^{17} cm^{-3} for Xenon for which the quenching rate would be ~1% of the TALIF spontaneous-decay rate, $A_{21,1}$). Absolute TALIF signal levels can be a critical challenge at sufficiently low densities, and signal generation in Kr will tend to be weaker than in Xe. To achieve similar levels, one requires about ~3-4x higher laser intensity for Kr to achieve a similar 2-photon rate as for Xe (for operation below saturation).

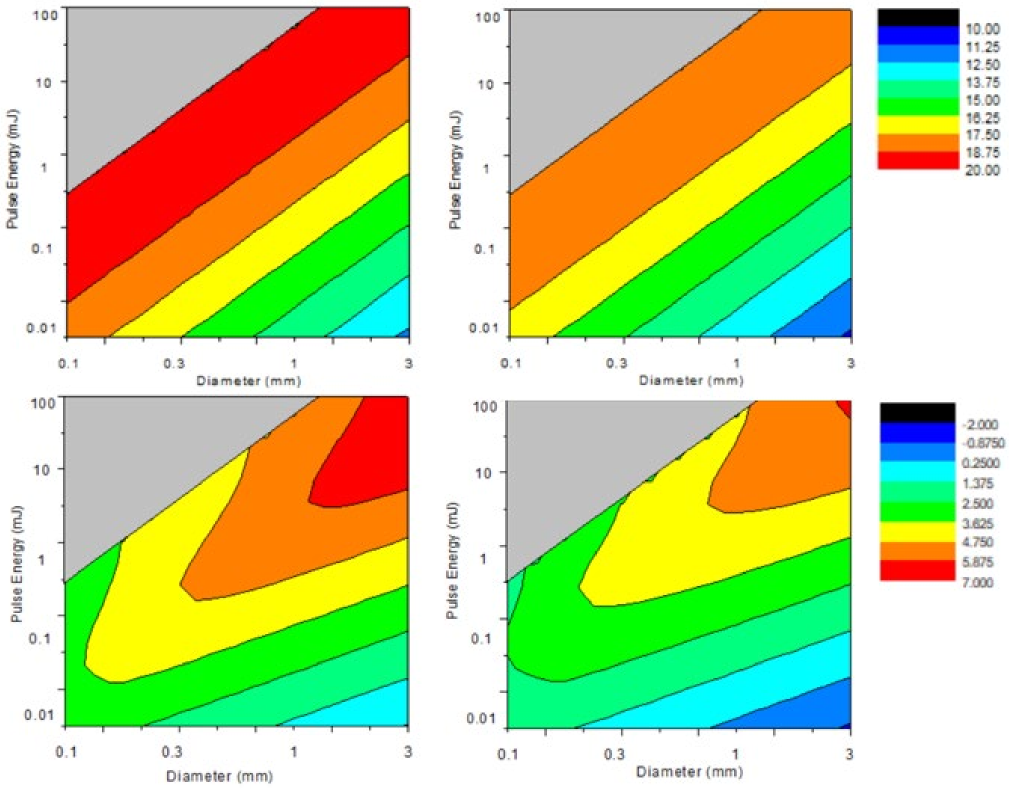

Xenon Krypton

Figure 7: Top: Surface plots of log₁₀ of peak fluorescence signal (# photons cm^{-3} s^{-1}) as function of beam diameter and pulse energy for xenon (left) and krypton (right) at density of 10^{12} cm^{-3}. Bottom: Surface plots of log₁₀ of total fluorescence signal (# of photons detected) for same conditions. The grey regions (top-left of each plot) are not computed due to high beam intensity (> 1 GW/cm^2).

C. Detection Issues for Plasma TALIF

A fundamental issue in applying TALIF to a plasma system is that the plasma inevitably tends to emit light (due to its own excitation) from the exact same transitions as are driven by the laser to generate the TALIF signal. Indeed, in the case of plasma thruster investigations, emission spectra do show measurable signals from the same lines used in our and other Xe and Kr schemes [7, 8, 45]. The high population of many of the xenon metastable states (lower levels of the fluorescent transitions) is also indicative of the strength of these lines (though lines where the lower state is not metastable are generally comparably strong in their emission). The strength of the competing emission has consequences in selecting the optimum spectral scheme as well as in the detailed experimental design (e.g. use of multiple blocking and/or bandpass filters or monochromator for light rejection [15, 16]). Even with filtering, the strong plasma emission can leak through the blocking filters leading to interferences [23] that can cause systematic errors if not accounted for. To date, there has been more application of Xe (versus Kr) TALIF for EP related research. Based on our past work, and the literature, we see no Xe plasma studies with 2-photon excitation at 252 nm or 249 nm. Instead, researchers have employed the 222.5 or 224.5 nm schemes [11-13, 46, 47] which seem favorable in plasma environments due to high cross-sections and branching ratios along with relatively weak plasma emission. More research to identify optimum schemes for detection in plasma, particularly for Krypton and other alternative propellants, is required.

Application of TALIF within plasmas can also be very revealing in terms of the fundamental processes. In particular, because the technique is specific to the ground state of neutral xenon, any ionization that reduces the neutral level will reduce the TALIF signal. Figure 8 shows TALIF absorption spectra recorded from same point within cold-flow in vacuum chamber and within plume of 1.5 kW HET. The spectra were recorded with the setup described in Section 3. Because the measurements are made at fixed laser energy, the area of the spectra are proportional to the xenon density in each case. The ionization fraction, Δ, at the measurement location within the HET plume can be inferred from the data through a ratio approach. The HET and cold-flow (CF) measurements were made at approximately equal chamber pressure, but during HET operation we have elevated temperature, $T_{HET,ON}$`, of the propellant. Assuming T_{CF}=300 K and $T_{HET,ON}$=400 K , and reading a signal ratio of $F_{Total,HET,ON}/F_{Total,CF}$ =0.25 from Figure 6 leads to an estimated ionization fraction of $\Delta = 0.67\ \left(= 1 - \left(F_{Total,HET-ON}/F_{Total,CF}\right)\left(T_{HET-ON}/T_{CF}\right)\right)$ in this case.

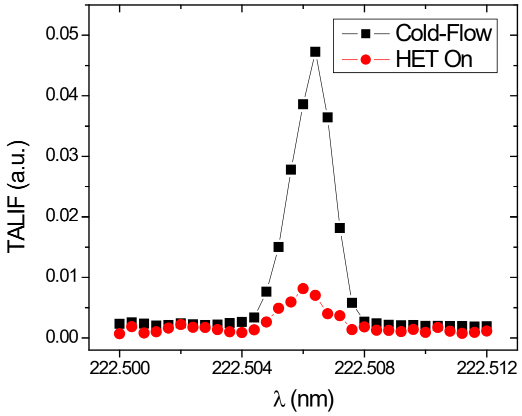

Figure 8: TALIF absorption spectra recorded from same point within cold-flow in vacuum chamber (labeled Plasma off) and within plume of 1.5 kW Hall thruster.

V. Conclusions

A 5-level rate model was proposed for studying the ground-state population via two-photon absorption laser induced fluorescence. The model is applied two TALIF schemes for Xe ($\lambda_{2\text{-Phton}}$=222.5 nm, λ_{Fluor}=788.7 nm) and Kr ($\lambda_{2\text{-Phton}}$=214.7 nm, λ_{Fluor}=760.2 nm) which are of interest for electric propulsion studies. The model showed that in both cases an increase in laser excitation intensity leads to three fluorescence regimes: (i) low intensity regime (I_{laser}<~10 MW/cm^2) where there is only weak excitation of level populations and most of the population remains in the ground state; (ii) intermediate intensity regime (10 MW/cm^2 <~ I_{laser} <~ 100 MW/cm^2), where the first saturation effects are first noticed (leading to a buildup of population in the fluorescence upper level); (iii) high intensity regime (I_{laser}>~100 MW/cm^2), where we notice significant photoionization via the absorption of a third photon (i.e., 2+1 REMPI). This is further confirmed when studying the impact of the focusing conditions which shows a decrease in fluorescence signal at high intensities (i.e., when the beam is strongly focused). From a practical point of view, it is interesting to note that, even though increasing the intensity beyond the intermediate regime doesn't lead to an increase in the total number of fluorescence photons, the fluorescence profile narrows and the peak intensity is reached faster. This could be successfully used to increase S/N ratio at low densities by using a narrower integration window (thus lowering the detection limit). Moreover, since the signal is completely decayed before the end of the laser pulse, the technique becomes essentially unaffected by quenching in the high-intensity regime (which is of interest in high-pressure plasma applications). By comparing Xe and Kr proposed schemes, we find that, for a fixed density, the TALIF signals for xenon are generally about an order of magnitude larger than those for krypton; however, if adequate laser sources are available then Kr signals can be increased to those due to Xe by increasing the laser energy (if saturation is avoided).

The proposed model is also validated against actual TALIF experimental data collected in our laboratory from running a 1.5 kW HET thruster using Xe. An exponential fit to the data gives a 1/e time of 26.9 ns which is within good agreement with the expected value of 28.6 ns (=1/$A_{21,1}$=1/3.5x10^7 s) given our experimental uncertainty. The model and experiments are also compared in terms of the dependence of TALIF signal on laser pulse energy. A discussion on the detection issues related to TALIF study in EP reveals the trade-offs between choosing a scheme with high cross-sections and branching ratios along with relatively weak plasma emission in the collection spectral region was presented. Finally, it is shown that by ratioing signals with and without plasma excitation, the TALIF spectra provide direct measures of ionization.

Acknowledgments

This work was partially supported by NASA through the Joint Advanced Propulsion Institute, a NASA Space Technology Research Institute, grant number 80NSSC21K1118. The authors acknowledge the help of Seth Thompson and Dr John Williams, from Colorado State University, in operating the Hall thruster and vacuum chamber used in this research.

References

1. Eckbreth, A.C., *Laser diagnostics for combustion temperature and species*. 1998, Kent, United Kingdom: Abacus Press.
2. Kinsey, J.L., *Laser-Induced Fluorescence.* Annual Review of Physical Chemistry, 1977. **28**(1): p. 349-372.
3. Goebel, D.M. and I. Katz, *Fundamentals of Electric Propulsion: Ion and Hall Thrusters*. JPL SPACE SCIENCE AND TECHNOLOGY SERIES. 2008, California Institute of Technology.
4. Huang, W., B. Drenkow, and A. Gallimore, *Laser-Induced Fluorescence of Singly-Charged Xenon Inside a 6-kW Hall Thruster*, in *45th AIAA/ASME/SAE/ASEE Joint Propulsion Conference & Exhibit*. 2009, American Institute of Aeronautics and Astronautics.
5. Young, C.V., et al., *Time-resolved laser-induced fluorescence diagnostics for electric propulsion and their application to breathing mode dynamics.* Plasma Sources Science & Technology, 2018. **27**(9).
6. Lee, D., N. Hershkowitz, and G.D. Severn, *Measurements of Ar+ and Xe+ velocities near the sheath boundary of Ar–Xe plasma using two diode lasers.* Applied Physics Letters, 2007. **91**(4): p. 041505.
7. Karabadzhak, G.F., Y.H. Chiu, and R.A. Dressler, *Passive optical diagnostic of Xe propelled hall thrusters. II. Collisional-radiative model.* Journal of Applied Physics, 2006. **99**(11): p. 12.
8. Chaplin, V.H., et al., *Insights from Collisional-Radiative Models of Neutral and Singly-Ionized Xenon in Hall Thrusters*, in *AIAA Propulsion and Energy 2021 Forum*. 2021, American Institute of Aeronautics and Astronautics.
9. Niemi, K., et al., *Absolute atomic oxygen and nitrogen densities in radio-frequency driven atmospheric pressure cold plasmas: Synchrotron vacuum ultra-violet high-resolution Fourier-transform absorption measurements.* Applied Physics Letters, 2013. **103**(3): p. 034102.
10. Göppert-Mayer, M., *Über Elementarakte mit zwei Quantensprüngen.* Annalen der Physik, 1931. **401**(3): p. 273-294.
11. Crofton, M., *Measurement of neutral xenon density profile in an ion thruster plume*, in *27th Plasma Dynamics and Lasers Conference*. 1996, American Institute of Aeronautics and Astronautics.
12. Eichhorn, C., et al. *Multi-Photon Spectroscopy on Xenon for Application on Ion Thruster Plasma Parameter Investigations: Experiment and Theory*. in *IEPC*. 2007. Florence, Italy: EPRS.
13. Crofton, M.W., et al., *Neutral Xenon Density in the SPT-140 Near-Field Plume*, in *International Electric Propulsion Conference*. 2013: Washington, D.C.
14. Kinefuchi, K., et al., *Two-photon absorption laser induced fluorescence with various laser intensities for density measurement of ground state neutral xenon.* Acta Astronautica, 2019. **161**: p. 382-388.
15. Wegner, J.T., *Two-Photon Absorption Laser Induced Fluorescence (Talif) Of Neutral Xenon In A Hall Effect Thruster Plasma*, in *Deparment of Mechanical Engineering*. 2021, Colorado State University: Fort Collins, CO.
16. Wegner, T., et al. *Two-Photon Absorption Laser Induced Fluorescence (TALIF) Of Neutral Xenon In A Hall Effect Thruster Plasma*. in *AIAA Propulsion & Energy Forum* 2021.
17. Hsu, A.G., et al., *Mixture fraction imaging in turbulent non-premixed flames with two-photon LIF of krypton.* Proceedings of the Combustion Institute, 2011. **33**(1): p. 759-766.
18. Narayanaswamy, V., R. Burns, and N.T. Clemens, *Kr-PLIF for scalar imaging in supersonic flows.* Optics Letters, 2011. **36**(21): p. 4185-4187.
19. Hsu, P.S., et al., *100 kHz PLEET velocimetry in a Mach-6 Ludwieg tube.* Optics Express, 2020. **28**(15): p. 21982-21992.
20. Jiang, N., et al., *High-repetition-rate krypton tagging velocimetry in Mach-6 hypersonic flows.* Applied Optics, 2022. **61**(9): p. 2192-2197.
21. Shekhtman, D., et al., *Freestream velocity-profile measurement in a large-scale, high-enthalpy reflected-shock tunnel.* Experiments in Fluids, 2021. **62**(5): p. 118.
22. Wang, Y., C. Capps, and W.D. Kulatilaka, *Femtosecond two-photon laser-induced fluorescence of krypton for high-speed flow imaging.* Optics Letters, 2017. **42**(4): p. 711-714.
23. Gazeli, K., et al., *Picosecond two-photon absorption laser-induced fluorescence (ps-TALIF) in krypton: The role of photoionization on the density depletion of the fluorescing state Kr 5p'[3/2]2.* Physics of Plasmas, 2021. **28**(4): p. 043301.
24. Galante, M.E., R.M. Magee, and E.E. Scime, *Two photon absorption laser induced fluorescence measurements of neutral density in a helicon plasma.* Physics of Plasmas, 2014. **21**(5): p. 055704.
25. Beebe, S.J. and K.H. Schoenbach, *Nanosecond pulsed electric fields: a new stimulus to activate intracellular signaling.* J Biomed Biotechnol, 2005. **2005**(4): p. 297-300.
26. Pointu, A.-M., et al., *Nitrogen Atmospheric Pressure Post Discharges for Surface Biological Decontamination inside Small Diameter Tubes.* Plasma Processes and Polymers, 2008. **5**(6): p. 559-568.

27. Mintusov, E., et al., *Mechanism of plasma assisted oxidation and ignition of ethylene–air flows by a repetitively pulsed nanosecond discharge.* Proceedings of the Combustion Institute, 2009. **32**(2): p. 3181-3188.
28. Niemi, K., V.S.-v.d. Gathen, and H.F. Döbele, *Absolute calibration of atomic density measurements by laser-induced fluorescence spectroscopy with two-photon excitation.* Journal of Physics D: Applied Physics, 2001. **34**(15): p. 2330-2335.
29. Goehlich, A., T. Kawetzki, and H.F. Döbele, *On absolute calibration with xenon of laser diagnostic methods based on two-photon absorption.* The Journal of Chemical Physics, 1998. **108**(22): p. 9362-9370.
30. Schmidt, J.B., et al., *Femtosecond, two-photon-absorption, laser-induced-fluorescence (fs-TALIF) imaging of atomic hydrogen and oxygen in non-equilibrium plasmas.* Journal of Physics D: Applied Physics, 2016. **50**(1): p. 015204.
31. Schmidt, J.B., et al., *Comparison of femtosecond- and nanosecond-two-photon-absorption laser-induced fluorescence (TALIF) of atomic oxygen in atmospheric-pressure plasmas.* Plasma Sources Science and Technology, 2017. **26**(5): p. 055004.
32. Dumitrache, C., et al., *Quantitative fs-TALIF in high-pressure NRP discharges: calibration using VUV absorption spectroscopy.* Plasma Sources Science and Technology, 2022. **31**(1): p. 015004.
33. Bamford, D.J., L.E. Jusinski, and W.K. Bischel, *Absolute two-photon absorption and three-photon ionization cross sections for atomic oxygen.* Physical Review A, 1986. **34**(1): p. 185-198.
34. Stancu, G.D., *Two-photon absorption laser induced fluorescence: rate and density-matrix regimes for plasma diagnostics.* Plasma Sources Science and Technology, 2020. **29**(5): p. 054001.
35. Kröll, S. and W.K. Bischel, *Two-photon absorption and photoionization cross-section measurements in the 5${p}^{5}$6p configuration of xenon.* Physical Review A, 1990. **41**(3): p. 1340-1349.
36. Horiguchi, H., R.S.F. Chang, and D.W. Setser, *Radiative lifetimes and two-body collisional deactivation rate constants in Ar for Xe(5p56p),Xe(5p56p), and Xe(5p57p) states.* The Journal of Chemical Physics, 1981. **75**(3): p. 1207-1218.
37. Dzierżęga, K., et al., *Accurate transition rates for the $5p\ensuremath{-}5s$ transitions in Kr I.* Physical Review A, 2000. **62**(2): p. 022505.
38. Shekhtman, D., M.A. Mustafa, and N.J. Parziale, *Two-photon cross-section calculations for krypton in the 190–220 nm range.* Applied Optics, 2020. **59**(34): p. 10826-10837.
39. Uddi, M., et al., *Atomic oxygen measurements in air and air/fuel nanosecond pulse discharges by two photon laser induced fluorescence.* Proceedings of the Combustion Institute, 2009. **32**(1): p. 929-936.
40. Kröll, S., et al., *Statistics of multimode YAG laser radiation with implications for quantitative coherent anti-Stokes Raman scattering spectroscopy in combustion diagnostics.* Journal of the Optical Society of America B, 1991. **8**(5): p. 930-939.
41. Hyman, H.A., *Photoionization cross sections for excited states of argon and krypton.* Applied Physics Letters, 1977. **31**(1): p. 14-15.
42. Alford, W.J., *State-to-state rate constants for quenching of xenon 6p levels by rare gases.* The Journal of Chemical Physics, 1992. **96**(6): p. 4330-4340.
43. NIST. *Atomic Spectra database.*
44. Miles, R.B., et al., *Microwave scattering from laser ionized molecules: A new approach to nonintrusive diagnostics.* Aiaa Journal, 2007. **45**(3): p. 513-515.
45. Nakles, M.R. and T.S. Matlock. *Hall Thruster Near-Field Plume Characterization Through Optical Emission Spectroscopy*. in *36th International Electric Propulsion Conference*. 2019. Vienna, Austria.
46. Eichhorn, C., et al., *Two-Photon Laser-Induced Fluorescence Diagnostics of a Radiofrequency Ion Thruster: Measurements in Xenon and Krypton*, in *International Electric Propulsion Conference*. 2019: Vienna, Austria.
47. Aanesland, A., et al., *Direct measurements of neutral density depletion by two-photon absorption laser-induced fluorescence spectroscopy.* Applied Physics Letters, 2007. **91**(12): p. 121502.